

Strategies for Corrosion Inhibition of Carbon Steel Pipelines Under Supercritical CO₂/H₂S Environments

Yoon-Seok Choi,^{‡*} Shokrollah Hassani,^{*} Thanh Nam Vu,^{*} Srdjan Nešić,^{*} Ahmad Zaki B. Abas,^{**} Azmi Mohammed Nor,^{**} and Muhammad Firdaus Suhor^{**}

The objective of the present study was to identify and quantify the key issues that affect the integrity of carbon steel in high-pressure CO₂ and CO₂/H₂S environments and to establish potential corrosion mitigation strategies using low Cr alloy steels and corrosion inhibitors. The experiments were performed in a 7.5 L autoclave with two combinations of CO₂ partial pressure and temperature (12 MPa/80°C and 8 MPa/25°C) with different H₂S concentrations (0 ppm, 100 ppm, and 200 ppm). The corrosion behavior of specimens was evaluated using electrochemical measurements and surface analytical techniques. Results showed that the addition of corrosion inhibitor decreased corrosion rate significantly from 90 mm/y to below 0.1 mm/y at supercritical CO₂ condition (12 MPa CO₂, 80°C). However, insufficient protection was achieved from low Cr alloy steels. The addition of small amounts of H₂S reduced the corrosion rate of carbon steel in high-pressure CO₂ environments. However, the corrosion rate was still higher than the targeted rate (<0.1 mm/y). Additional protection was required in order to achieve the target. Utilizing 400 ppm of an imidazoline-type corrosion inhibitor reduced the corrosion rate of carbon steel below 0.1 mm/y in a high-pressure CO₂ condition with H₂S. Compared to carbon steel, the corrosion resistance of low Cr steels was lower in the corresponding CO₂ conditions with H₂S.

KEY WORDS: carbon steel, CO₂/H₂S corrosion, corrosion inhibitor, low Cr steel, supercritical CO₂

INTRODUCTION

Numerous studies on corrosion issues in high-pressure CO₂ environments relating to carbon capture and storage, enhanced oil recovery, and deep water oil and gas production applications have recently been published.¹⁻⁸ The published literature primarily addresses topics related to CO₂ sequestration and enhanced oil recovery that usually involve “dry” gases where water is only present at the ppm level.⁹⁻¹⁴ However, due to the direct impact of the presence of formation water and high-pressure CO₂ on the corrosion of pipeline steel, the aqueous corrosion rate of carbon steel at high-CO₂ pressure (liquid and supercritical CO₂) without the formation of protective FeCO₃ corrosion product layers is very high (>20 mm/y).¹⁵⁻¹⁹

For corrosion control, sufficient gas “drying” (water removal) upstream of the pipeline is required in order to prevent breaking-out of free water and excessive corrosion rates.²⁰⁻²¹ However, it can be too costly to dry the gas stream in the field conditions. As the aqueous corrosion mechanisms of carbon steel are similar under both low-CO₂ pressure and high-CO₂ pressure,²²⁻²³ using corrosion inhibitors (CIs) and/or corrosion resistant alloys (CRAs) could be a promising strategy in order to control corrosion at high-pressure CO₂ conditions.¹

The performance of various CIs in the CO₂-saturated aqueous solutions has been widely studied. Imidazoline-based inhibitors are the mostly used formulations in the oil and gas field to control CO₂ corrosion. However, the studies were usually conducted under low-CO₂ pressure related to typical conditions seen in oil and gas pipelines. For high-CO₂ pressure

conditions, publications that report on efficiencies of corrosion inhibitors in supercritical CO₂ systems are sparse.^{1,24} Classic corrosion inhibitor formulations based on imidazoline, piperazine, alkenylsuccinic acids, and quaternary ammonium compounds were evaluated in supercritical CO₂ systems.²⁵⁻²⁷ Although these chemicals did reduce the corrosion rate, none of them were fully effective. In previous research,²⁸ an attempt was made to control the corrosion of carbon steel in high-pressure CO₂ conditions (8 MPa CO₂ and 70°C) using imidazoline-based CIs. The study showed that adequate protection was achieved by applying “imidazoline + thiosulfate” CI blend to carbon steel in the high-pressure CO₂ environments.

As the use of CRAs remains very expensive, there has been an attempt to use low-Cr alloy steel (0.5% to 3% Cr) in high-pressure and high-temperature CO₂ environments without inhibitor injection.²⁹⁻³⁰ This has the potential to significantly reduce costs associated with the use of CRAs for infrastructure construction.

It has recently been reported that small amounts of H₂S can be present in high-pressure CO₂ streams related to gas field development.³¹⁻³² Even though the effect of H₂S on the aqueous corrosion of carbon steel at low CO₂ partial pressures is widely investigated,³³⁻³⁴ limited work has been done in high-pressure CO₂ environments.^{32,35-37} In addition, there is no systematic study on corrosion inhibition strategy in high-pressure CO₂ environments with H₂S.

Thus, the objective of the present study was to identify and quantify the key issues that affect the integrity of carbon steel in high-pressure CO₂ and CO₂/H₂S environments and to establish potential corrosion mitigation strategies using low-Cr

Submitted for publication: January 23, 2018. Revised and accepted: June 28, 2019. Preprint available online: June 28, 2019, <https://doi.org/10.5006/2765>.

[‡] Corresponding author. E-mail: choiy@ohio.edu.

^{*} Institute for Corrosion and Multiphase Technology, Department of Chemical and Biomolecular Engineering, Ohio University, Athens, Ohio 45701.

^{**} Petronas Research SDN. BHD, Selangor Darul Ehsan, Malaysia.

Table 1. Chemical Compositions of Materials Used in the Present Study (wt%, balance Fe)

	C	Cr	Mn	P	S	Si	Cu	Ni	Mo	Al
CS	0.065	0.05	1.54	0.013	0.001	0.25	0.04	0.04	0.007	0.041
1Cr	0.3	0.85	0.91	0.015	0.008	0.29	–	–	–	–
3Cr	0.08	3.43	0.54	0.006	0.003	0.30	0.16	0.06	0.32	–

Table 2. Chemical Composition of the Corrosion Inhibitor Packages

Product	Description	Active ingredient	Components
Cl1	Inhibitor blend	tail oil fatty acid/diethylenetriamine (TOFA/DETA) imidazoline + Sodium thiosulfate	10% CH ₃ COOH
			13% C ₄ H ₉ OCH ₂ CH ₂ OH
			20% TOFA/DETA imidazoline
			6.28% Na ₂ S ₂ O ₃ ·5H ₂ O
			Balance water
Cl2	Generic inhibitor	tail oil fatty acid/diethylenetriamine (TOFA/DETA) imidazoline	10% CH ₃ COOH
			13% C ₄ H ₉ OCH ₂ CH ₂ OH
			24% TOFA/DETA imidazoline
			Balance water

alloy steels and CIs for achieving targeted corrosion rate (<0.1 mm/y).

EXPERIMENTAL PROCEDURES

The materials used in this work are as follows:

- UNS K03014⁽¹⁾ carbon steel, named CS
- UNS G41300-1Cr steel, named 1Cr
- UNS G41300-3Cr steel, named 3Cr

The chemical compositions of the studied alloys analyzed using atomic emission spectroscopy are shown in Table 1. The test specimens were machined with two different geometries: cylindrical type with 5 cm² exposed area for electrochemical measurements, and rectangular type with a size of 1.27 cm × 1.27 cm × 0.254 cm for surface analysis. The specimens were ground sequentially with 250, 400, then 600-grit silicon carbide (SiC) paper, cleaned with isopropyl alcohol in an ultrasonic bath, and dried.

In the present study, "imidazoline + thiosulfate" corrosion inhibitor blend (Cl1) and "imidazoline" generic corrosion inhibitor (Cl2) were selected for evaluation under high-pressure CO₂ environments with and without H₂S based on the results of preliminary tests.²⁸ In this instance, "imidazoline" is shorthand for tall oil fatty acid (TOFA) imidazoline-type inhibitor. The formulation of the corrosion inhibitor packages is shown in Table 2.³⁸

The corrosion experiments were carried out in a 7.5-L autoclave (UNS N10276) which contained a working electrode, a high pressure/high temperature Ag/AgCl reference electrode and a platinum coated niobium counter electrode. A schematic of the experimental setup is shown in Figure 1. The electrolyte was a 1 wt% NaCl solution. The solution volume to specimen surface area was 420 mL/cm². An impeller was used to stir the solution at a rotation speed of 1,000 rpm (approximately corresponding to 1 m/s); stirring was maintained during the test.

The experimental procedure is outlined in Figure 2. Initially, 1 wt% of NaCl solution was placed in an autoclave and this electrolyte purged with a high flow rate of CO₂ for 1 h to 3 h in order to remove dissolved O₂. The electrodes and specimens were then placed in the autoclave. After closing the autoclave, temperature was increased to the testing temperature. Once the working temperature was achieved, additional purging with CO₂ or a mixture of CO₂/10% H₂S was performed for 1 h to 2 h to ensure the removal of O₂ and the saturation of CO₂ or CO₂/H₂S, and then the working H₂S partial pressure was achieved by pressurizing with the mixture of CO₂/10% H₂S for the CO₂/H₂S conditions. High-pressure CO₂ was then injected with a booster pump.

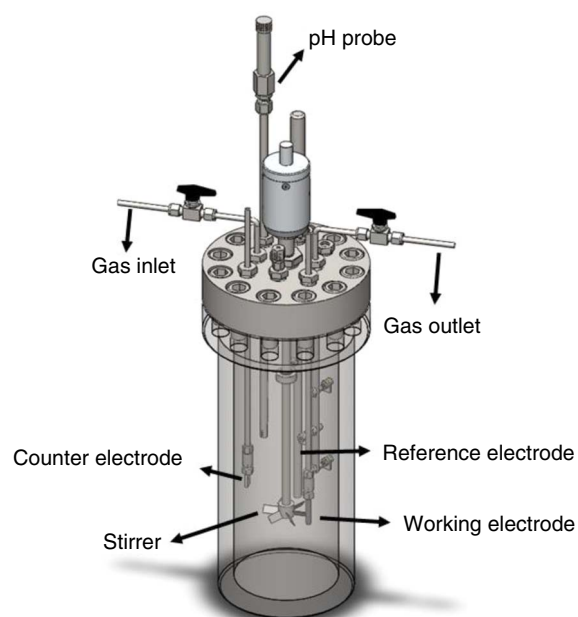


FIGURE 1. Schematic of autoclave system equipped for electrochemical measurements.

⁽¹⁾ UNS numbers are listed in *Metals and Alloys in the Unified Numbering System*, published by the Society of Automotive Engineers (SAE International) and cosponsored by ASTM International.

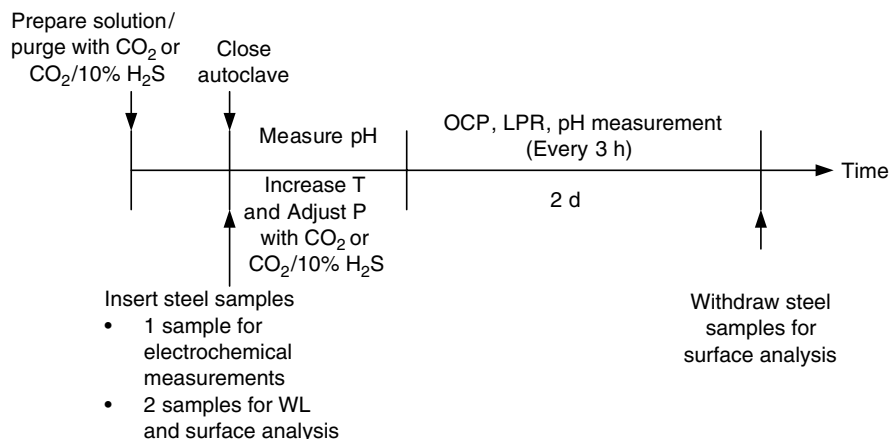


FIGURE 2. Experimental procedures for evaluating the corrosion behavior of materials in high-pressure CO₂ environments with H₂S.

In order to ensure that no oxygen contamination occurred during the test, indirect evidences were checked at the end of each test:

- No change of color for the solution was observed. If the system was contaminated with oxygen, the solution color should change to orange due to the formation of iron oxide.
- Elemental sulfur could form when the system has both H₂S and O₂. In the present tests, elemental sulfur was not observed in the autoclave.
- Iron oxide was not detected in the corrosion product.

During the experiment, corrosion rates and corrosion potentials were monitored with linear polarization resistance (LPR) measurement made at regular time intervals using the range of ±5 mV with respect to the open circuit potential, and a scan rate of 0.125 mV/s. The polarization resistance (R_p) obtained from LPR measurement was used to calculate the corrosion current density (i_{corr}) by using Equation (1):

$$i_{corr} = \frac{B}{R_p} = \frac{\beta_a \times \beta_c}{2.3 \times R_p \times (\beta_a + \beta_c)} \quad (1)$$

where β_a is the anodic Tafel constant and β_c is the cathodic Tafel constant. In the present study, empirical B value of 23 mV for the CO₂-H₂S corrosion was used for all conditions.³⁹ Then, the i_{corr} was converted into corrosion rate using Equation (2):

$$\text{Corrosion rate (mm/year)} = \frac{0.00327 \times i_{corr} (\mu\text{A/cm}^2) \times EW}{\text{density (g/cm}^3)} \quad (2)$$

where EW is the equivalent weight in grams and 0.00327 is a constant factor used for dimension and time conversion.

During the experiment, the solution pH was measured periodically by using commercial high-pressure glass pH

Condition	CO ₂ Pressure (MPa)	H ₂ S (ppm)	Temperature (°C)
CO ₂	12	0	80
	12	100	80
	12	200	80
CO ₂ /H ₂ S	8	100	25
	8	200	80

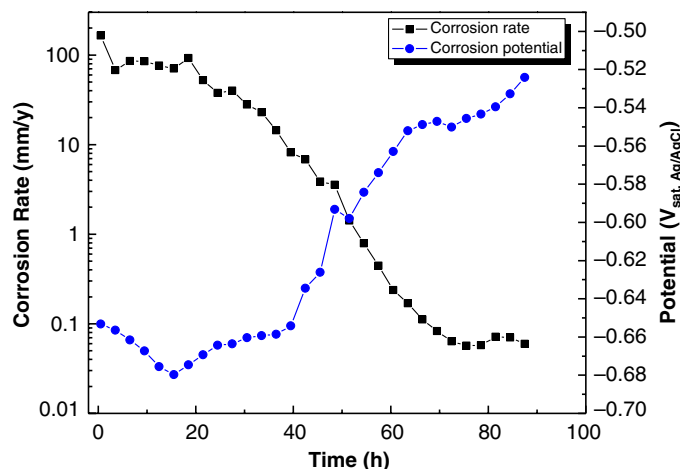


FIGURE 3. Corrosion rate and corrosion potential of CS in CO₂ saturated 1 wt% NaCl solution at 12 MPa CO₂ and 80°C.

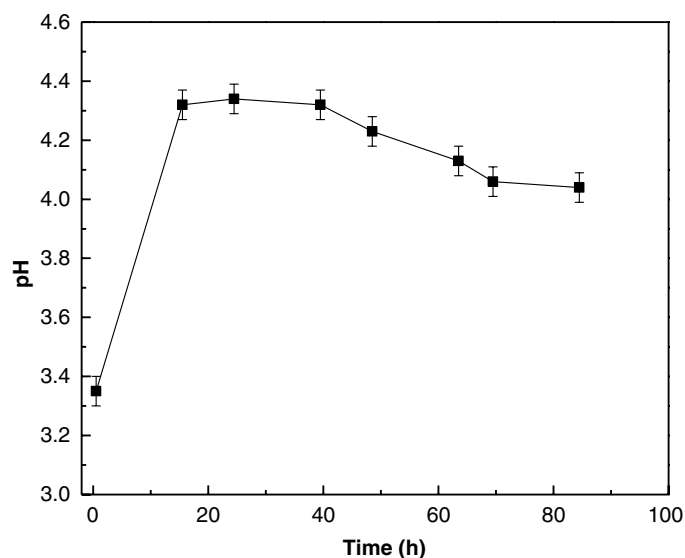


FIGURE 4. pH measurement data during corrosion experiment of CS in CO₂ saturated 1 wt% NaCl solution at 12 MPa and 80°C.

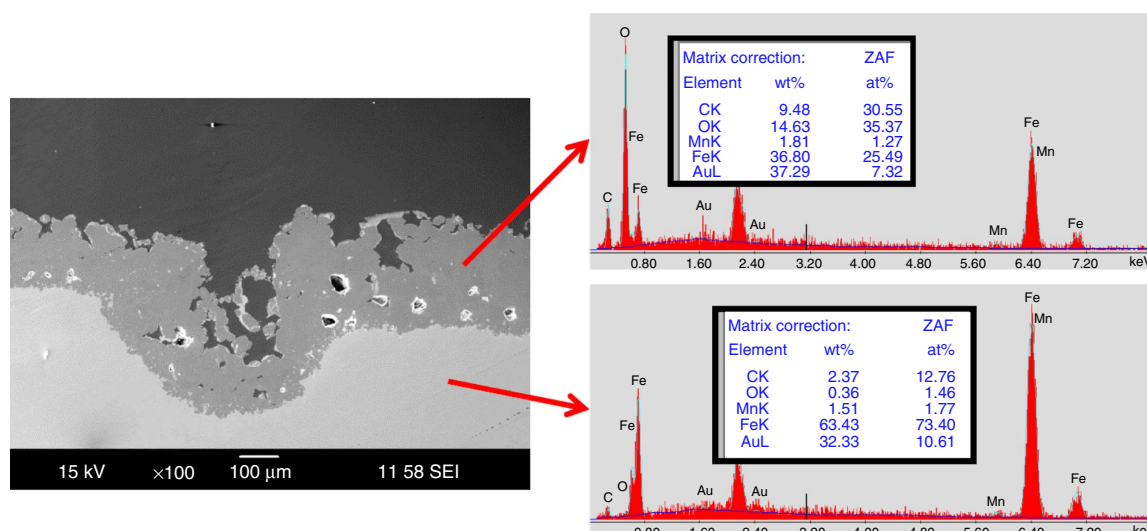


FIGURE 5. SEM and EDS cross-sectional analysis of CS in CO₂ saturated 1 wt% NaCl solution at 12 MPa and 80°C.

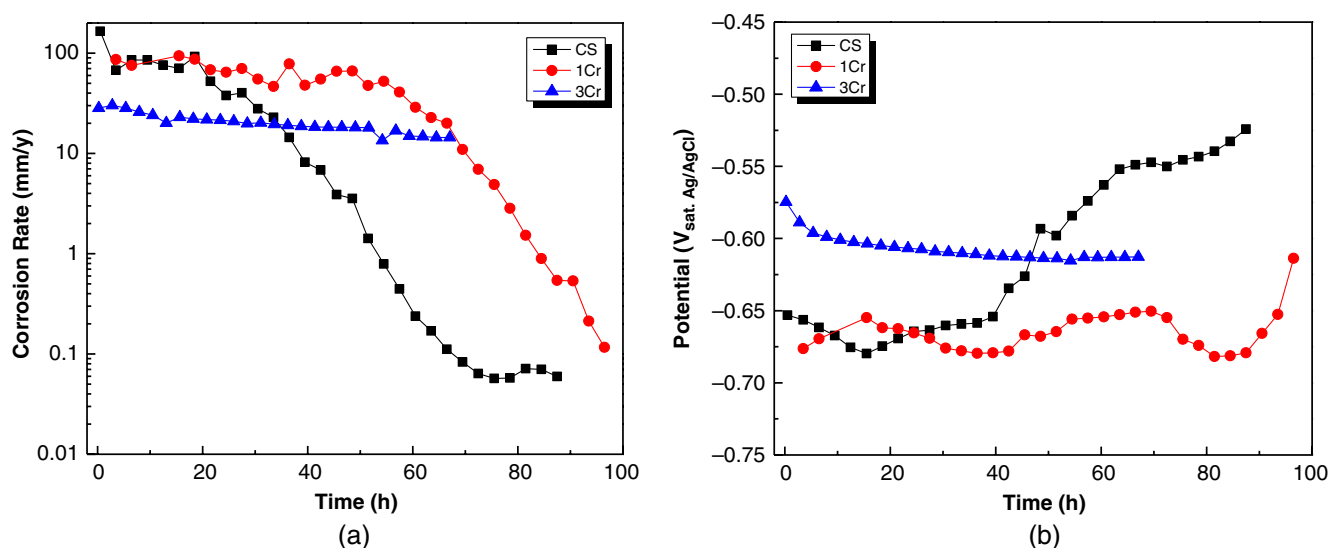


FIGURE 6. LPR data of CS, 1Cr, and 3Cr steels in CO₂ saturated 1 wt% NaCl solution at 120 bar and 80°C: (a) corrosion rate and (b) corrosion potential.

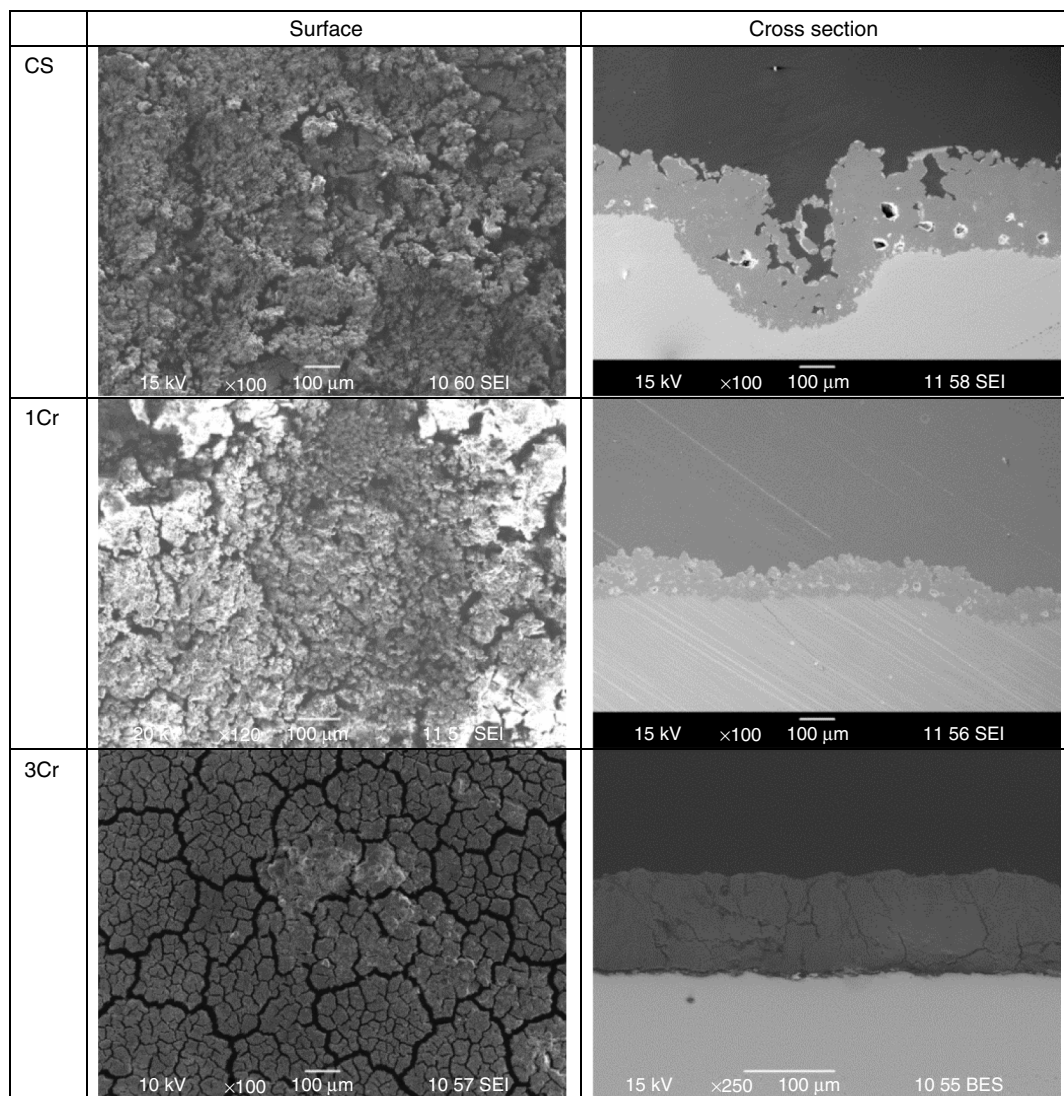


FIGURE 7. SEM surface and cross-section analysis of CS, 1Cr, and 3Cr steels after corrosion experiment at 12 MPa and 80°C in CO₂ saturated 1 wt% NaCl solution.

electrode and Ag/AgCl reference electrode. The electrodes were calibrated prior to each test by the procedure supplied by the manufacturer.⁴⁰

After each test, the specimens were removed from the autoclave, rinsed with DI water and isopropyl alcohol, dried with N₂ and stored in a desiccator cabinet in an inert atmosphere until surface analyses could be conducted. The surface morphology and compositions of corrosion products were analyzed with scanning electron microscopy (SEM), energy

Table 4. EDS Surface Analysis of CS, 1Cr, and 3Cr steels after Corrosion Experiment in CO₂ Saturated 1 wt% NaCl Solution at 12 MPa and 80°C

Element	CS (at%)	1Cr (at%)	3Cr (at%)
C	31	42	66
O	35	28	17
Cr	0	1.3	13
Fe	25	29	2

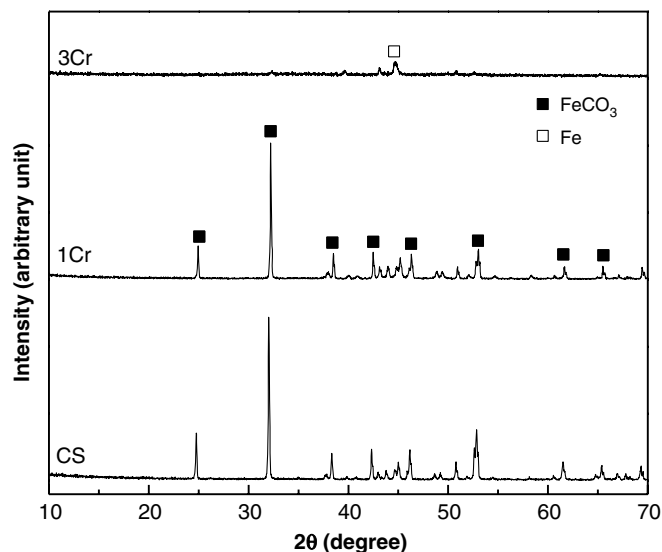


FIGURE 8. Result of XRD analysis for CS, 1Cr, and 3Cr steels exposed to 12 MPa CO₂ and 80°C.

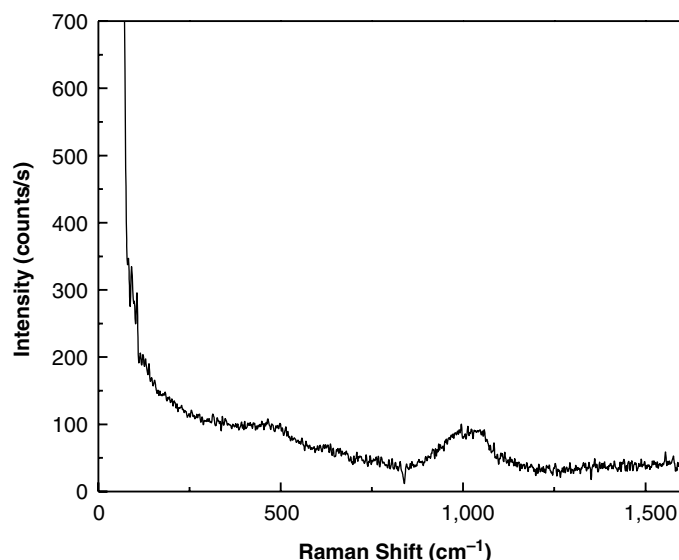


FIGURE 9. Result of Raman spectroscopy analysis for 3Cr steel exposed to 12 MPa CO₂ and 80°C.

dispersive x-ray spectroscopy (EDS), x-ray diffraction (XRD), and Raman spectroscopy. In addition, the cross-sectional SEM and EDS analysis were performed by using the samples cold-mounted in the epoxy. For testing with inhibitors, the procedure was the same as shown in Figure 2, except the inhibitor was added to the solution before inserting the specimens.

Table 3 shows the test conditions for the present study. The test conditions were set in order to simulate the inlet and outlet conditions for CO₂ transportation pipeline, where the CO₂ is present in a supercritical state at the "inlet" condition and it exists as a liquid at the "outlet" condition.³¹ For the CO₂ environments, the corrosion behavior and inhibition strategy were evaluated at the inlet condition, whereas it was investigated at both inlet and outlet conditions for the CO₂/H₂S environments.

RESULTS AND DISCUSSION

3.1 | Corrosion Inhibition Strategies Under High-Pressure CO₂ Environments

Figure 3 shows the variations of corrosion rate and corrosion potential for CS with time under 12 MPa CO₂ and 80°C. The corrosion rate of CS is about 90 mm/y at the beginning of the experiment and then sharply decreases after 20 h. In addition, the corrosion potential increased when the corrosion rate started to decrease. This indicates that protective iron carbonate (FeCO₃) layers formed on the steel surface. pH values were also monitored during the experiment, as shown in Figure 4. pH data represent the bulk pH of the solution, which suggests a considerable change in bulk water chemistry because of initial high corrosion rate and the small volume of solution in the autoclave. This considerable change in water chemistry is

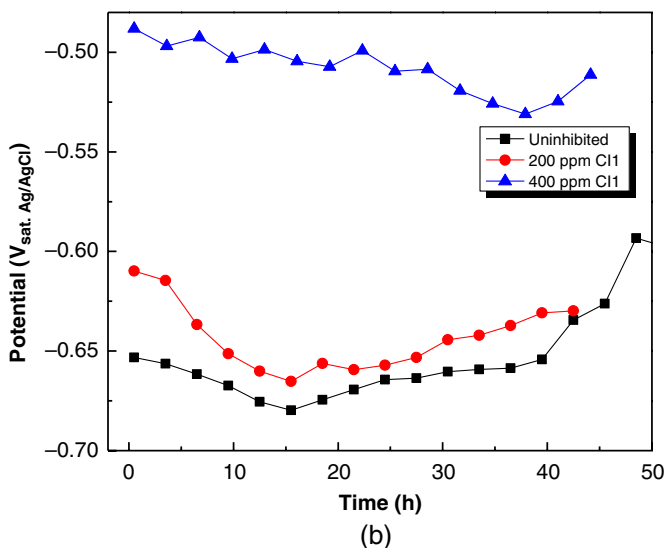
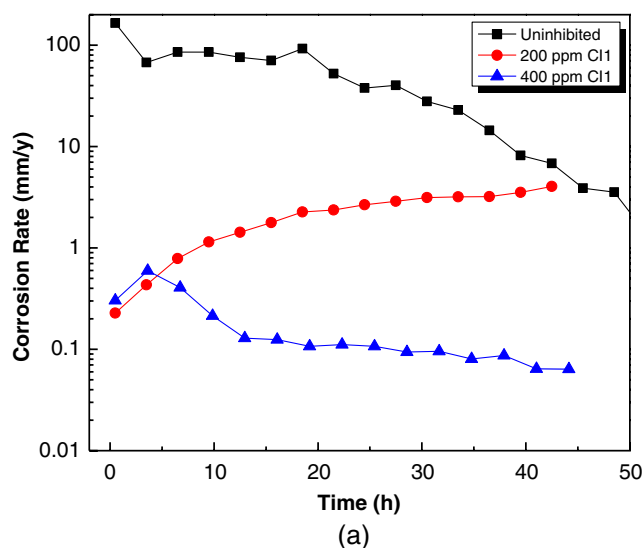


FIGURE 10. LPR data of CS with different concentrations of inhibitor in CO₂ saturated 1 wt% NaCl under 12 MPa and 80°C: (a) corrosion rate and (b) corrosion potential.

responsible for the drop in corrosion rate after 20 h of experimentation. Cross-sectional analysis using SEM and EDS (Figure 5) shows the formation of FeCO_3 layer on the steel surface, which caused the drop in corrosion rate. However, in actual field conditions, this considerable change in water chemistry would not be happening because at any given location in the line the water is being continuously replenished. Therefore, it must be stated that in this case, the decrease in

corrosion rate because of changes in water chemistry and formation of FeCO_3 is an artifact of experimental design.^{22,41-42} Therefore, the initial measured corrosion rate of 90 mm/y is the best representative of the corrosion rate of CS at 12 MPa and 80°C expected in the field conditions.

Figure 6 shows the corrosion behavior of different materials (CS, 1Cr, and 3Cr) at 12 MPa and 80°C. 3Cr steel shows a lower corrosion rate compared with CS and 1Cr steel at the

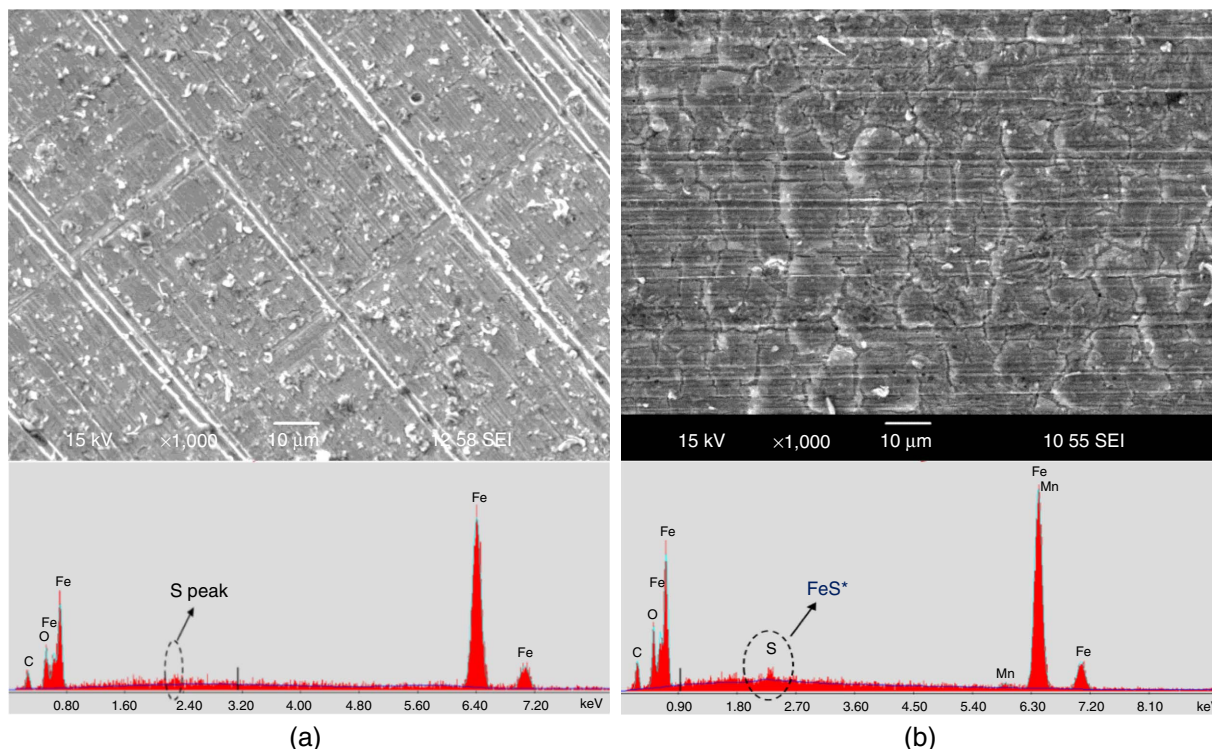


FIGURE 11. SEM images and EDS analysis of the CS sample surfaces after the inhibition tests with different Cl concentrations at 12 MPa and 80°C: (a) 200 ppm Cl1 and (b) 400 ppm Cl1.

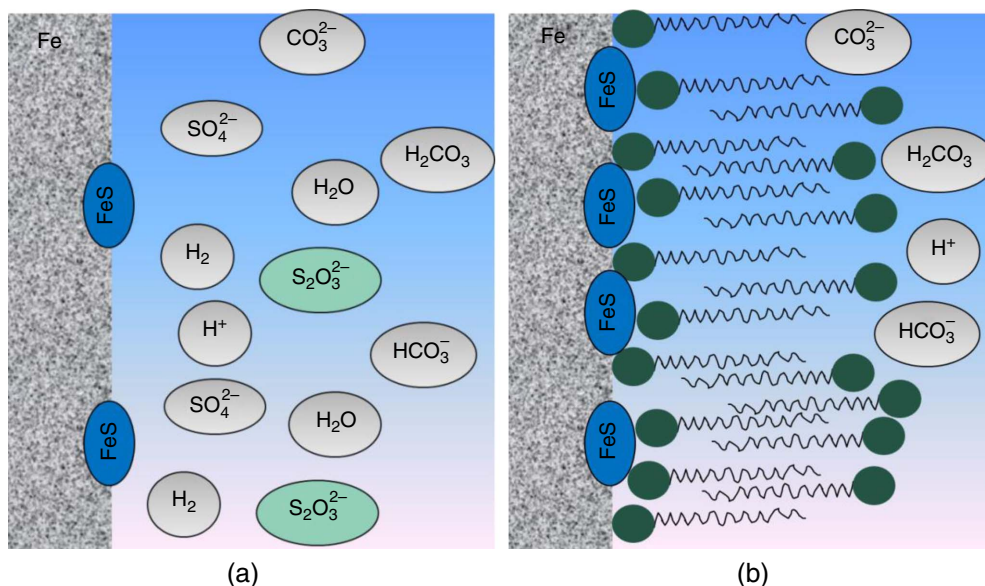


FIGURE 12. Hypothesis for the inhibition mechanism in pure CO₂ environment: (a) Step 1-formation of FeS from thiosulfate and (b) Step 2-adsorption of the imidazoline derivative (green head group with inhibitor tail) on FeS.

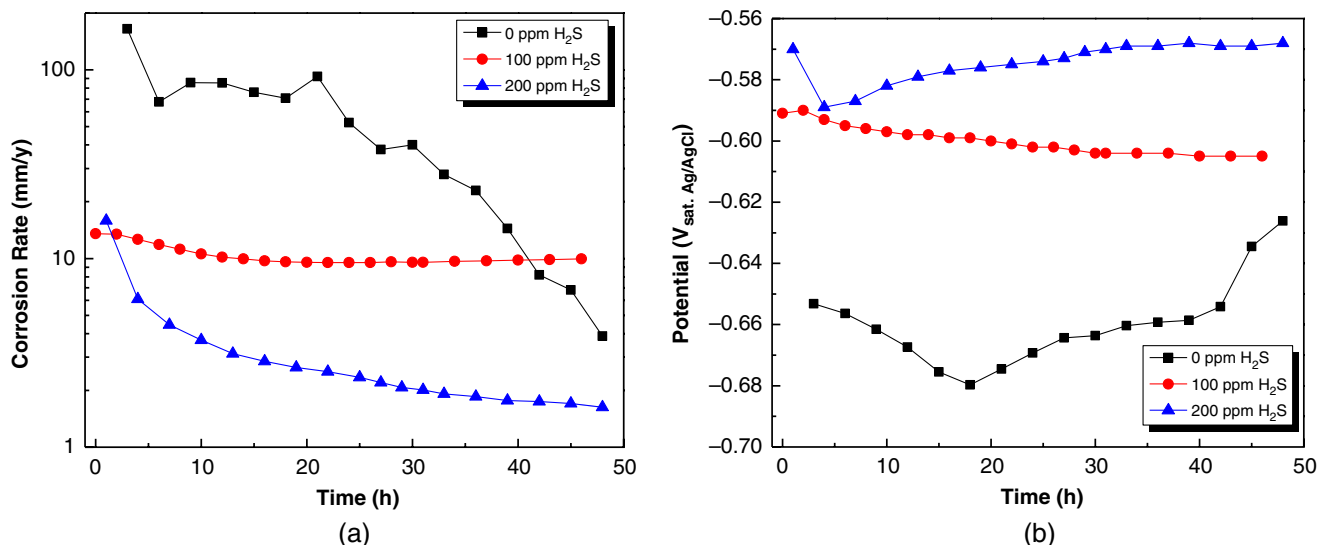


FIGURE 13. LPR data of CS in CO₂ saturated brine containing 0 ppm, 100 ppm, and 200 ppm H₂S at 12 MPa CO₂ and 80°C: (a) corrosion rate and (b) corrosion potential.

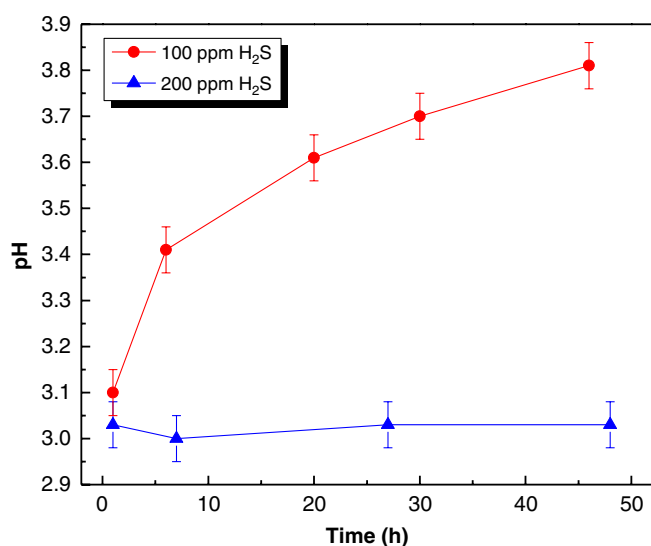


FIGURE 14. pH measurement data during corrosion experiment of CS in CO₂ saturated 1 wt% NaCl solution at 12 MPa and 80°C with 100 ppm and 200 ppm H₂S.

beginning of the experiment. CS and 1Cr showed similar corrosion performance under this condition. CS and 1Cr showed a drop in corrosion rate and increase in corrosion potential after a few days because of the abovementioned experimental artifact relating to changes in water chemistry of bulk solution and formation of FeCO₃. However, the 3Cr steel showed a lower corrosion rate from the very beginning of the experiment, which means that some sort of protective layer immediately formed on the surface. It should be noted that this "lower" corrosion rate was still catastrophically high (30 mm/y).

Surface analysis (SEM, EDS, and XRD) was conducted to better understand the performance of materials at this condition (Figure 7, Table 4, and Figure 8). 3Cr steel forms a thick corrosion products on the surface, which is not really protective because of the corrosion rate of 20 mm/y at the

end of the experiment. This layer is Cr-rich, based on the EDS analysis shown in Table 4 but XRD only shows a weak peak of Fe. Therefore, this layer is amorphous as well as being chromium-rich. Raman spectroscopy analysis (Figure 9) detected a strong peak at around 1,000 cm⁻¹ originates from the O-H deformation and, thus, can be used as a fingerprint for identifying corrosion products of 3Cr steel as chromium hydroxide, Cr(OH)₃. Formation of Cr(OH)₃ is very fast and can reduce the corrosion rate, but is insufficiently protective to reduce the corrosion rate significantly under this condition.

Corrosion rates and corrosion potentials of CS at 12 MPa and 80°C in CO₂ saturated 1 wt% NaCl solution with the presence of 0 ppm, 200 ppm, and 400 ppm of Cl1 are shown in Figure 10. With the presence of 200 ppm of Cl1, the initial corrosion rate was much lower than the uninhibited condition, however, the corrosion rate increased with time, indicating insufficient inhibition for the Cl1 concentration of 200 ppm. With 400 ppm of Cl1, the corrosion rate decreased with time to below 0.1 mm/y with more noble corrosion potential, which is the targeted inhibited corrosion rate.

The results of the surface analysis for samples after corrosion experiments with different concentrations of Cl1 are shown in Figure 11. On the sample surfaces with 200 ppm and 400 ppm of Cl, there was a very thin layer of corrosion products containing sulfur, possibly FeS formed indirectly via disproportionation of the thiosulfate component in the inhibitor. There is a stronger peak of S with 400 ppm of Cl1 because of the doubled thiosulfate concentration for the 400 ppm experiment compared to that conducted for 200 ppm of Cl1.

Based on the current understanding and the experimental results above, we propose an inhibition mechanism for high-CO₂ aqueous environment, having two main steps:

- Step 1 (Figure 12[a]): As CO₂ saturated aqueous solution is acidic, thiosulfate (one of the main component of inhibitor) disproportionates to form sulfide which rapidly reacts with Fe to form FeS on the steel surface, as summarized by the following reaction:⁴³



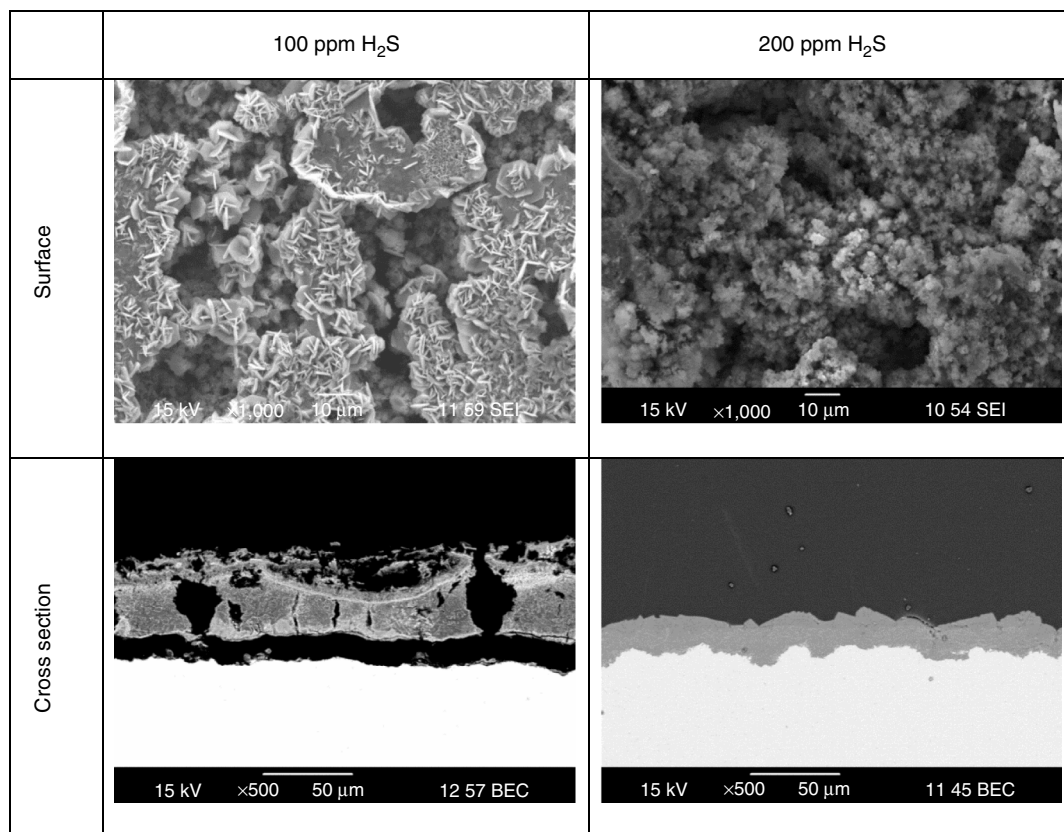


FIGURE 15. SEM surface and cross-sectional analyses of CS after corrosion experiment at 12 MPa CO₂ and 80°C with different H₂S concentrations.

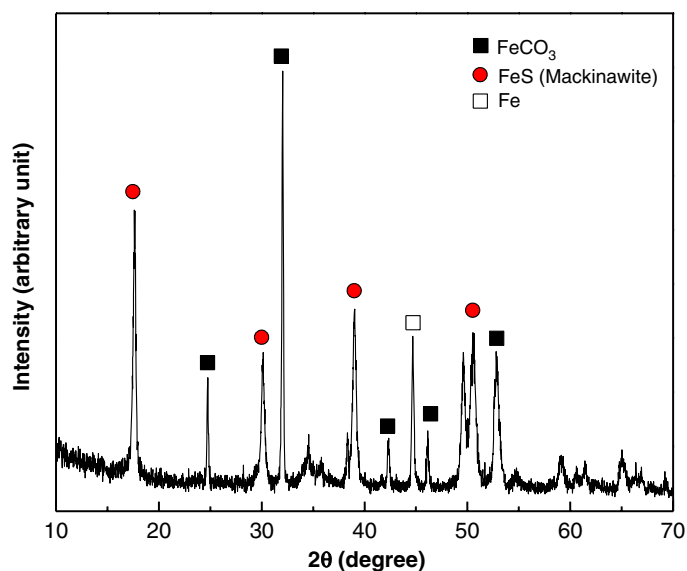


FIGURE 16. Result of XRD analysis for CS exposed to 12 MPa CO₂ and 80°C with 200 ppm H₂S.

It is assumed that this process is very fast based on the kinetics of the FeS formation reaction (order of seconds and minutes).

- Step 2 (Figure 12[b]): Following the formation of a thin layer of FeS on the steel surface, adsorption of the imidazoline (the main component of the

inhibitor) would happen. The adsorption kinetics is much slower (order of hours). Moreover, the adsorption of the organic inhibitors on the steel surface covered by a thin FeS layer has been hypothesized to be stronger than on the bare steel surface.

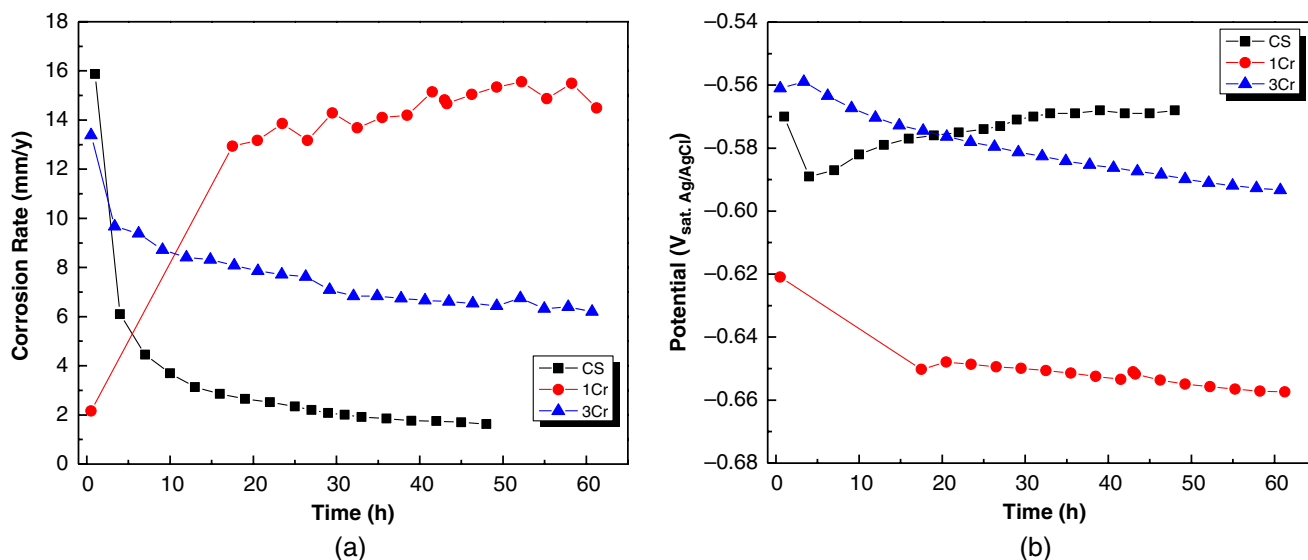


FIGURE 17. LPR data of different materials in CO₂ saturated brine containing 200 ppm H₂S at 12 MPa CO₂ and 80°C: (a) corrosion rate and (b) corrosion potential.

3.2 | Corrosion Inhibition Strategies Under High-Pressure CO₂ Environments with H₂S: Inlet Condition (12 MPa, 80°C)

Figure 13 shows the variations of corrosion rate and corrosion potential with time under different H₂S concentrations. With the presence of 100 ppm of H₂S, the initial corrosion rate was much lower than in the pure CO₂ condition, and the corrosion rate and corrosion potential were constant with time. This indicates that the addition of a small amount of H₂S reduced the corrosion rate almost 10 times under high-pressure CO₂ conditions. With 200 ppm of H₂S, the corrosion rate also starts out initially with similar values as for the case with 100 ppm H₂S, and then decreased to a low value, in the range of 1 mm/y to 2 mm/y. Figure 14 shows the change of pH during the experiments in the presence of H₂S. Unlike the pure CO₂ condition (Figure 4), the solution pH was constant for the condition with 200 ppm H₂S indicating that bulk water chemistry has not appreciably changed. Therefore, the corrosion rate decrease, in this case, is not an artifact of the experimentation and the same result would have obtained in a field condition.

Figure 15 shows the surface and cross-section SEM images of the corroded samples after 2 d at 12 MPa CO₂ and 80°C with different H₂S concentrations. In the presence of 200 ppm H₂S, the corrosion product layer is more compact and adherent to the metal surface, providing better corrosion protection. Figure 16 shows the XRD pattern of the corrosion product layer formed at 12 MPa and 80°C with 200 ppm H₂S. The layer formed in this condition showed a combination of FeS and FeCO₃.

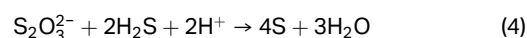
Although the addition of H₂S provided a certain degree of protection to CS in the high-pressure CO₂ condition, the corrosion rate was still high and it required additional protection in order to achieve the targeted inhibited corrosion rate (<0.1 mm/y). Figure 17 shows LPR corrosion data of CS, 1Cr, and 3Cr steels in the CO₂/H₂S system. It is interesting to note that CS shows the lowest corrosion rate in comparison with 1Cr and 3Cr steels. The 1Cr steel shows very active behavior in the CO₂/H₂S system with high corrosion rate and low corrosion potential. The result suggests that no beneficial effect of Cr is

observed at these conditions (12 MPa CO₂ and 80°C) with 200 ppm H₂S, contrary to the case of the pure CO₂ system.

SEM and EDS surface analysis of specimens after corrosion experiments was conducted and the results are shown in Figure 18 and Table 5. CS formed a compact corrosion product layer, which is a combination of FeS and FeCO₃ and reduces the corrosion rate. However, 1Cr and 3Cr steels formed a Cr-rich layer on the surface (Table 5), which could be identified as Cr(OH)₃.⁴⁴ It can be hypothesized that this layer reduces the adherence of the FeS layer to the metal surface, and, consequently compromises the corrosion resistance.⁴⁵ Adherence of corrosion product layer to the metal surface is a key element in corrosion protectiveness of corrosion product layers. Furthermore, the severe localized attack was observed on the surface of 1Cr steel.

ClIs were added to reduce the corrosion rate of CS in high-pressure CO₂ with H₂S. Corrosion behavior of CS with different ClIs in the CO₂/H₂S environment (12 MPa, 80°C, 200 ppm H₂S) is shown in Figure 19. The concentration of the ClIs was fixed at 400 ppm based on the above result in the pure CO₂ environments. Although both ClIs showed similar inhibition performance at the beginning of the test, only Cl2 ("imidazole" generic) reduced the corrosion rate to lower than 0.1 mm/y at the end of the test.

According to the surface analysis, Figure 20, a significant amount of corrosion products were found on the sample with Cl1 whereas no visible corrosion attack was observed on the surface with Cl2. In the presence of Cl1, the corrosion products contain high amounts of sulfur (S) (Table 6). This can be postulated to be due to the formation of elemental S resulting from the reaction between thiosulfate and H₂S, as described by Siu and Jia:⁴⁶



This formation of elemental S could be a reason for insufficient inhibition with Cl1. Furthermore, localized corrosion with a maximum depth of around 150 μm was observed after removing corrosion product using Clarke's solution (20 g antimony trioxide, 50 g stannous chloride, and hydrochloric acid to make 1,000 mL) on the sample with Cl1 (Figure 21).

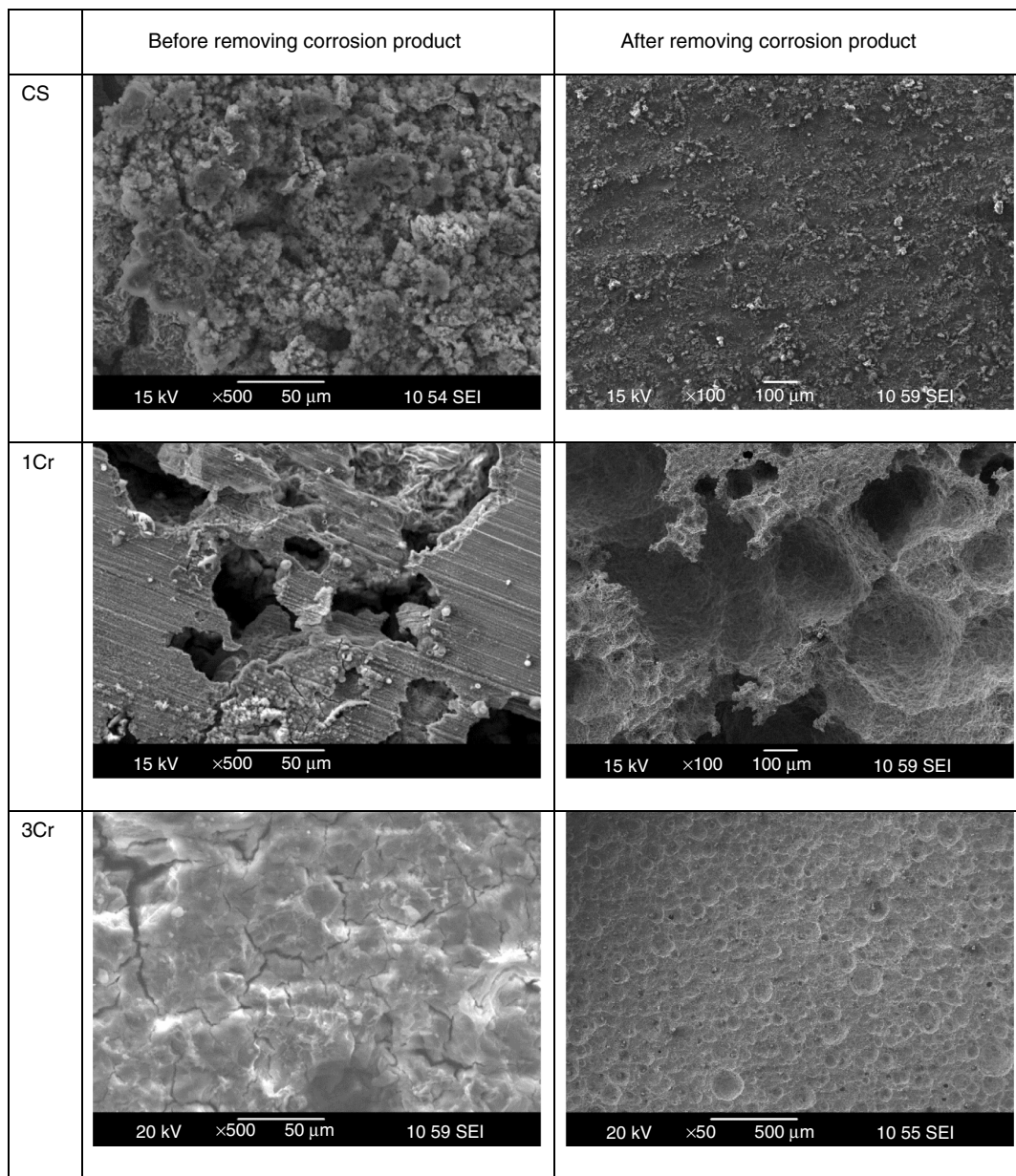


FIGURE 18. SEM surface analysis of different materials after corrosion experiments in NaCl electrolyte at 12 MPa CO₂ and 80°C with 200 ppm H₂S.

Table 5. EDS Surface Analysis of Materials After Corrosion Experiment in CO₂ Saturated 1 wt% NaCl Solution at 12 MPa CO₂ Containing 200 ppm H₂S and Temperature of 80°C

Element	CS (at%)	1Cr (at%)	3Cr (at%)
C	28	37	20
O	39	6	27
S	6	3	10
Cr	0	36	36
Fe	22	53	7

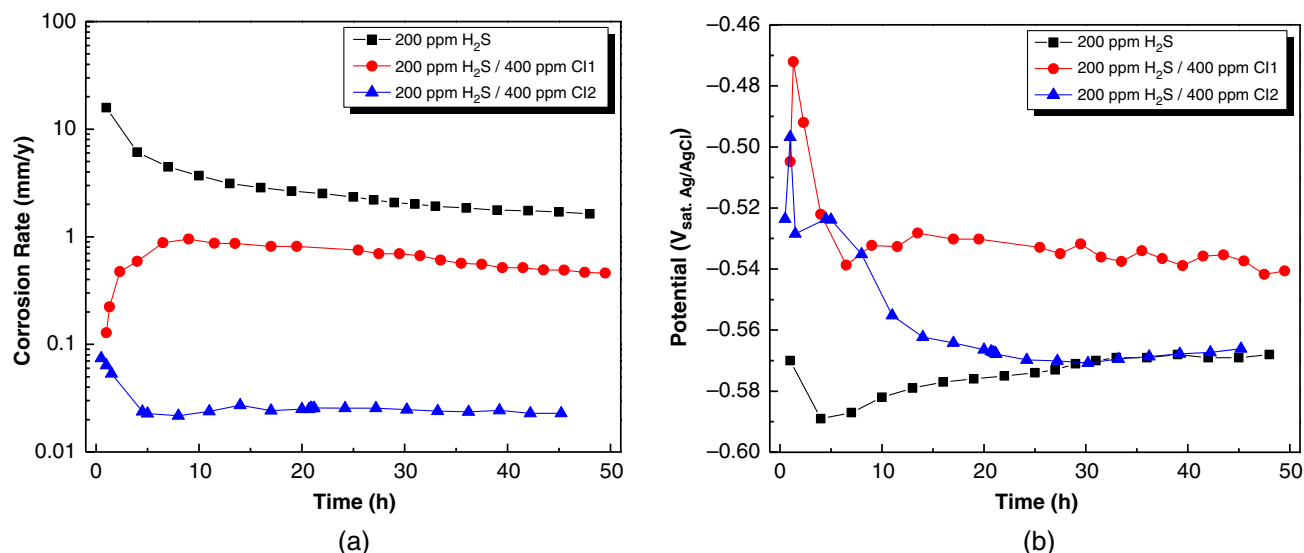


FIGURE 19. LPR data of CS in CO₂ saturated brine with and without CIs at 12 MPa CO₂ and 80°C (200 ppm H₂S): (a) corrosion rate and (b) corrosion potential.

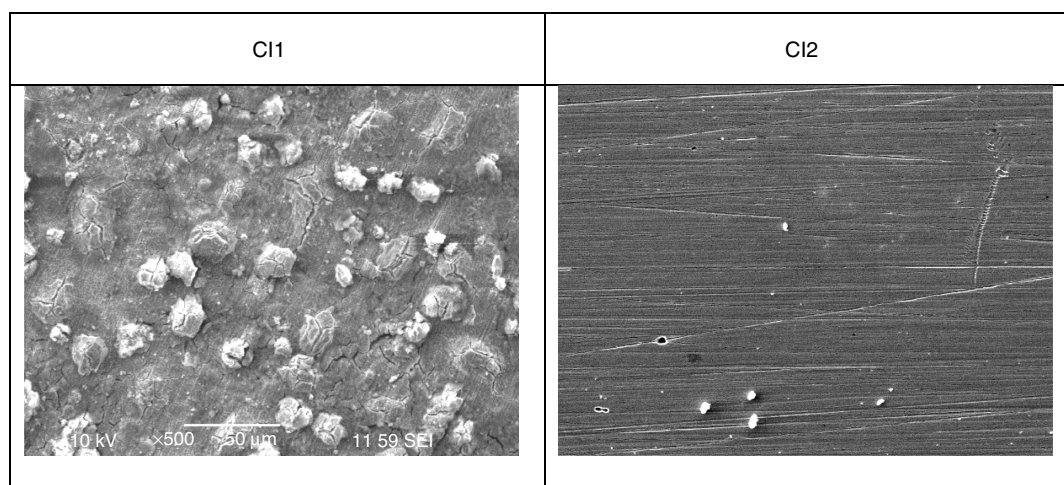


FIGURE 20. SEM images of the sample surface in CO₂ saturated 1 wt% NaCl solution with the presence of 400 ppm of inhibitors at 12 MPa and 80°C (200 ppm H₂S): (a) CI1 and (b) CI2.

Table 6. EDS Surface Analysis of the Sample After Corrosion Experiments with CI1 and CI2 at 12 MPa CO₂ and 80°C (200 ppm H₂S)

Element	CI1 (at%)	CI2 (at%)
C	52	18
O	11	2
S	11	1
Fe	20	79

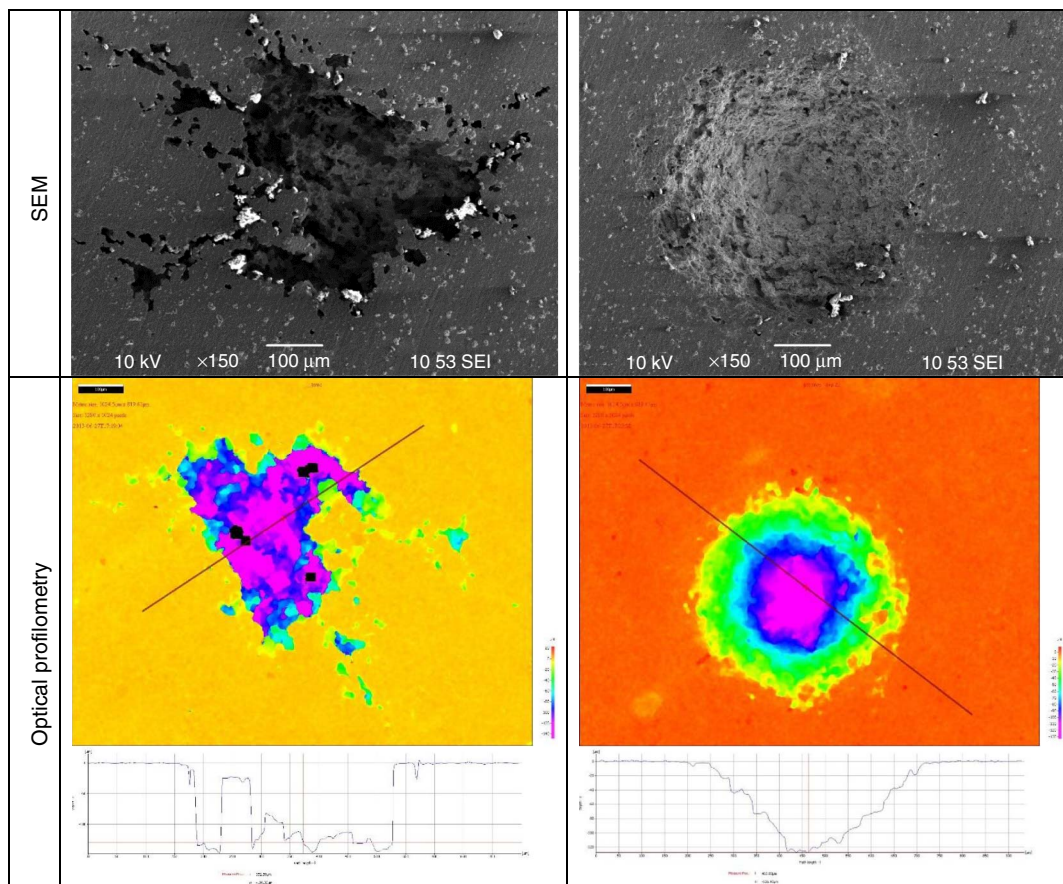


FIGURE 21. SEM and optical profilometry analysis of the CS sample surface in CO₂ saturated 1 wt% NaCl solution with the presence of 400 ppm of Cl1 at 12 MPa and 80°C (200 ppm H₂S).

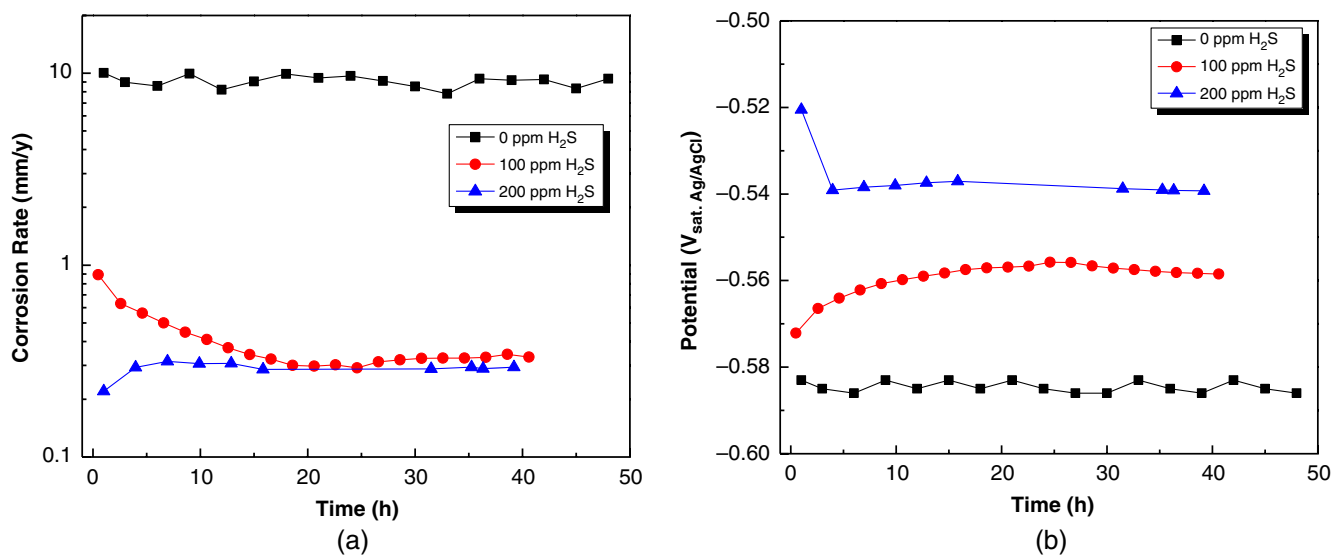


FIGURE 22. LPR data of CS in CO₂ saturated brine containing 0 ppm, 100 ppm, and 200 ppm H₂S at 8 MPa CO₂ and 25°C: (a) corrosion rate and (b) corrosion potential.

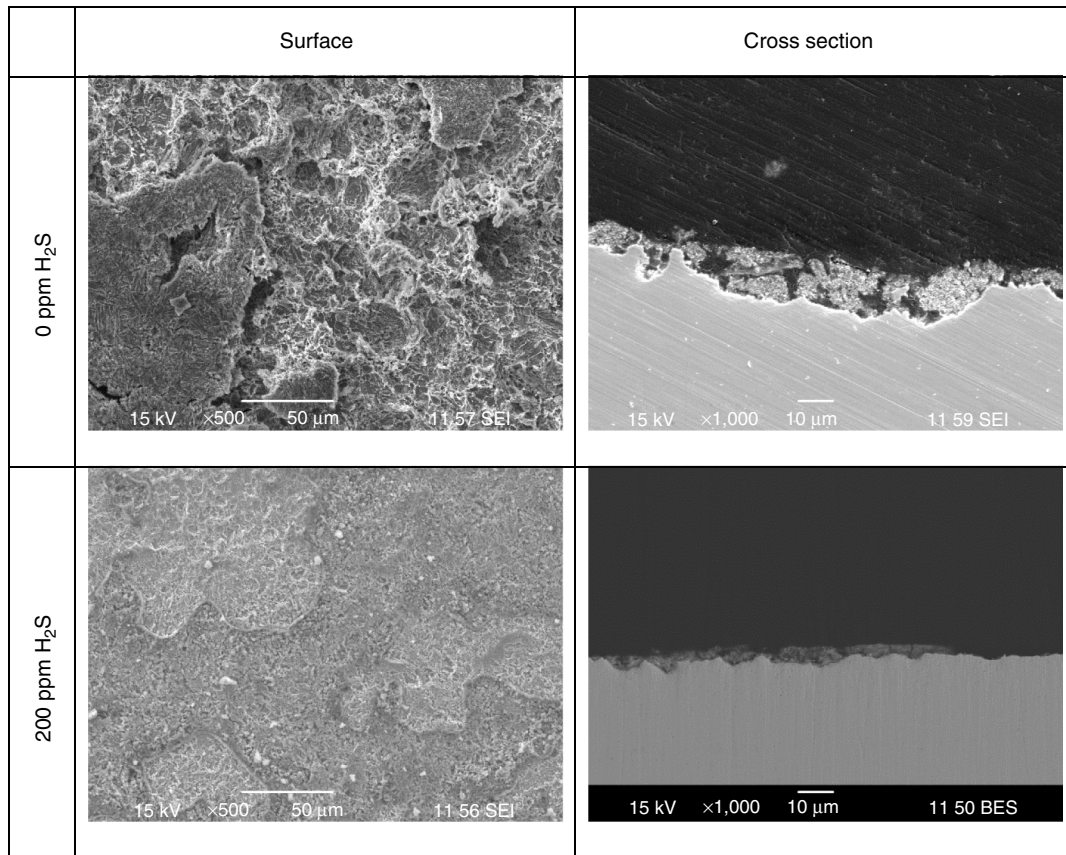


FIGURE 23. SEM and EDS surface analysis of CS after corrosion experiment at 8 MPa CO₂ and 25°C with different H₂S concentrations.

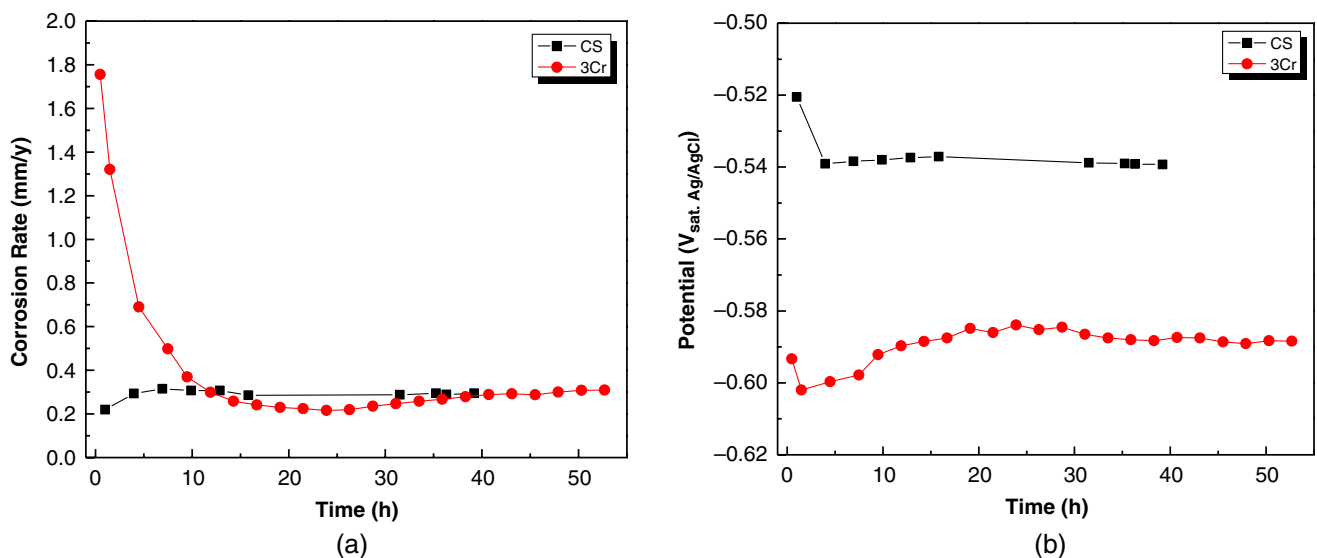


FIGURE 24. LPR data of different materials in CO₂ saturated brine containing 200 ppm H₂S at 8 MPa CO₂ and 25°C: (a) corrosion rate and (b) corrosion potential.

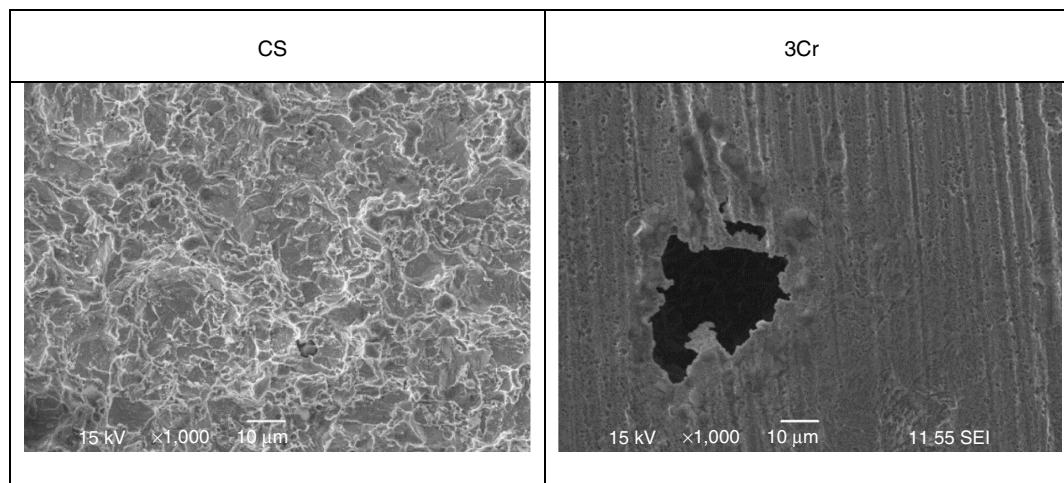


FIGURE 25. SEM images of CS and 3Cr steel after removing corrosion products.

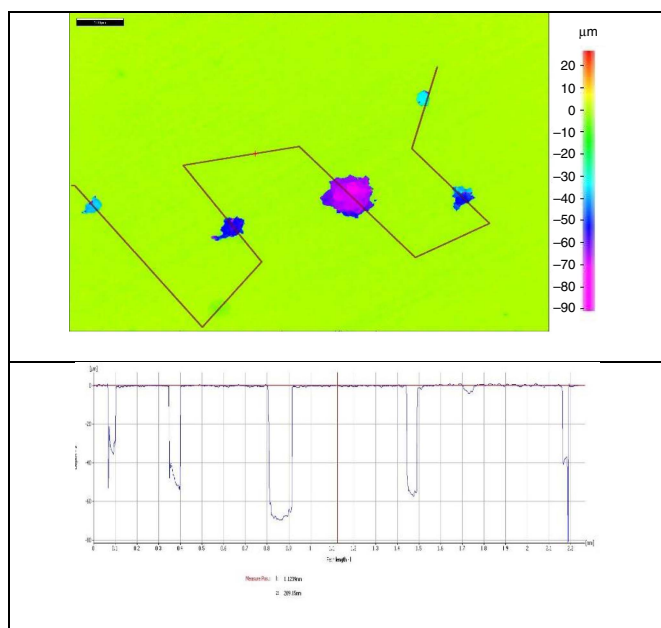


FIGURE 26. Optical profilometry analysis of 3Cr steel after corrosion experiment in brine system at 80 bar CO_2 pressure containing 200 ppm H_2S and temperature of 25°C.

3.3 | Corrosion Inhibition Strategies Under High-Pressure CO_2 Environments with H_2S : Outlet Condition (8 MPa, 25°C)

Corrosion rates and corrosion potentials of CS at 8 MPa and 25°C in CO_2 saturated 1 wt% NaCl electrolyte with the presence of 0 ppm, 100 ppm, and 200 ppm of H_2S are shown in Figure 22. Without H_2S , the corrosion rate is constant at about 10 mm/y from the beginning to the end of the experiment. With the presence of H_2S , again the corrosion rate was lower than the pure CO_2 condition. Although the corrosion rate with 200 ppm H_2S starts at a lower value than the case with 100 ppm H_2S , the corrosion rates for both conditions show similar values of around 0.3 mm/y after 15 h.

SEM surface and cross-section analysis for the effect of H_2S at 8 MPa and 25°C is shown in Figure 23. CS is unable to form a FeCO_3 corrosion product layer at 25°C. Therefore, the

absence of this FeCO_3 at 25°C means there is no as protectiveness due to corrosion product layer formation, as occurred at the inlet condition (12 MPa and 80°C). In the system without H_2S , there was only a small amount of iron carbide (Fe_3C) on the surface; this is a residue of cementite in the steel when corrosion dissolved the ferrite phase. With 200 ppm H_2S , the surface was covered by a thin but more adherent S-containing corrosion product, which provides corrosion protection.

Figure 24 shows LPR corrosion data of CS and 3Cr steel in the 1 wt% NaCl electrolyte at 8 MPa CO_2 and 25°C with 200 ppm H_2S . CS showed lower corrosion rate from the very beginning of the experiment, which means that a protective FeS layer immediately formed on the surface. However, 3Cr steel showed a drop in corrosion rate after a few hours then reached a stable corrosion rate similar to CS. The LPR results suggest that at the outlet condition, 3Cr steel shows a comparable corrosion performance with CS in a $\text{CO}_2/\text{H}_2\text{S}$ system.

Figure 25 shows the SEM surface analysis of CS and 3Cr steel after removing corrosion product using Clarke's solution. In the case of CS, SEM surface analysis shows uniform corrosion attack on the surface. However, it shows that localized corrosion occurs for 3Cr steel. High-resolution optical profilometry was used to study the depth of the surface features associated with the observed localized corrosion attack. Figure 26 shows the results of high-resolution optical profilometry analysis of several pits observed on the cleaned 3Cr steel exposed to 8 MPa CO_2 and 25°C with 200 ppm H_2S . According to the depth of the deepest pits, the maximum localized corrosion rate was measured to be 8 mm/y, which is 26 times higher than the general corrosion rate.

The corrosion rate and corrosion potential of CS as a function of time with and without H_2S and Cl_2 in the outlet condition are shown in Figure 27. The addition of 200 ppm of H_2S decreased corrosion rate significantly from about 10 mm/y to about 0.3 mm/y, and the addition of Cl_2 in the $\text{CO}_2/\text{H}_2\text{S}$ environment decreased the corrosion rate to much lower values (less than 0.1 mm/y).

SEM surface analysis of the sample surface before and after removing corrosion products once again confirms the superior inhibition performance of Cl_2 in the outlet condition (Figure 28).

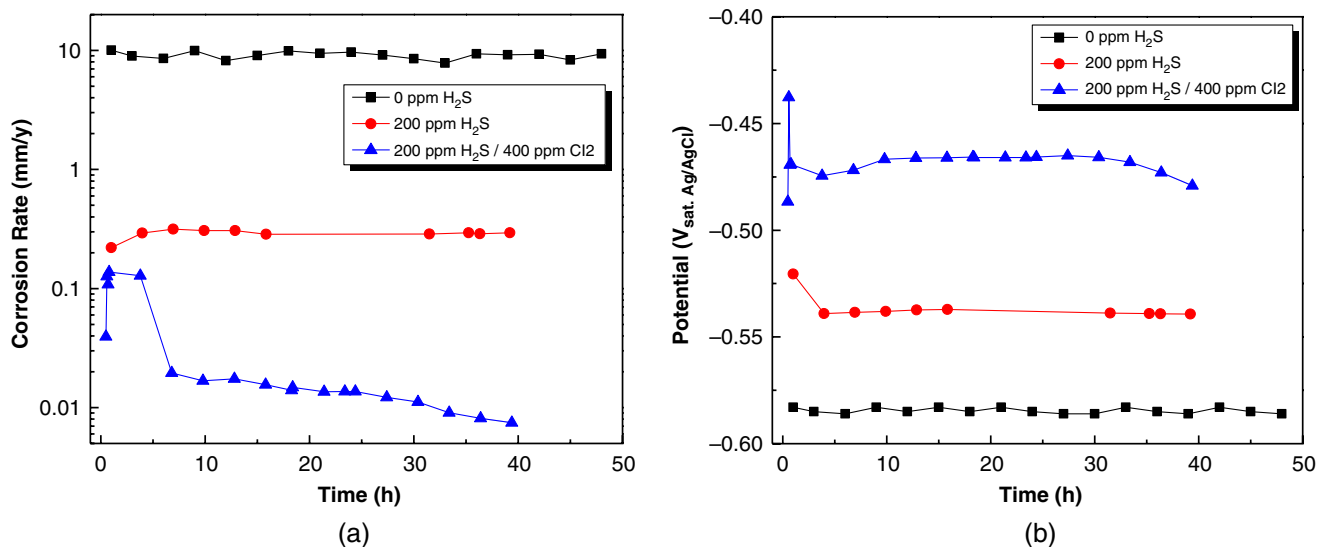


FIGURE 27. LPR data of CS in CO₂ saturated brine with and without H₂S and Cl₂ at 8 MPa CO₂ and 25°C: (a) corrosion rate and (b) corrosion potential.

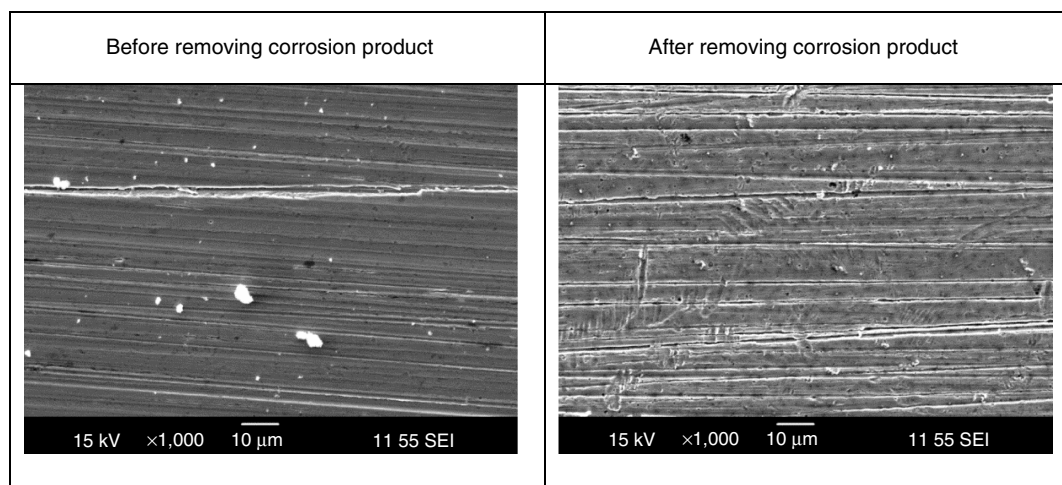


FIGURE 28. SEM images of the sample surface in CO₂ saturated 1 wt% NaCl solution with the presence of 400 ppm of Cl₂ at 8 MPa CO₂ and 25°C with 200 ppm H₂S.

CONCLUSIONS

The corrosion mechanisms and corrosion protection of CS in a high-pressure CO₂/H₂S system at different conditions were investigated by conducting electrochemical measurements and using surface analytical techniques. The following conclusions are drawn:

- At least 400 ppm of corrosion inhibitor was needed in order to control the aqueous corrosion rate below 0.1 mm/y at 12 MPa CO₂ and 80°C condition.
- Insufficient protection was achieved from low-Cr alloy steels at 12 MPa CO₂ and 80°C condition.
- The presence of small amounts of H₂S reduces the corrosion rate of CS in high-pressure CO₂ conditions.
- The corrosion resistance of low Cr steels was worse than that of CS in high-pressure CO₂ condition with some H₂S, indicating that applications of low Cr steels are limited to low-pressure CO₂ condition.

- Adding 400 ppm of imidazoline-type corrosion inhibitor can be utilized in order to reduce the corrosion rate of CS below 0.1 mm/y in high-pressure CO₂ conditions with some H₂S.

References

1. S. Sim, I.S. Cole, Y.S. Choi, N. Birbilis, *Int. J. Greenhouse Gas Control* 29 (2014): p.185.
2. L. Wei, Y. Zhang, X. Pang, K. Gao, *Corros. Rev.* 33 (2015): p. 151.
3. S. Sarrade, D. Feron, F. Rouillard, S. Perrin, R. Robin, J.C. Ruiz, H.A. Turc, *J. Supercritical Fluids* 120 (2017): p. 335.
4. Y. Xiang, M. Xu, Y.S. Choi, *Corros. Eng. Sci. Technol.* 52 (2017): p. 485.
5. R. Barker, Y. Hua, A. Neville, *Int. Mater. Rev.* 62 (2017): p. 1.
6. Y. Hua, R. Jonnalagadda, L. Zhang, A. Neville, R. Barker, *Int. J. Greenhouse Gas Control* 64 (2017): p. 126.
7. C. Sun, J. Sun, Y. Wang, P. Sui, X. Lin, H. Liu, X. Cheng, M. Zhou, *Int. J. Greenhouse Gas Control* 65 (2017): p. 117.
8. L. Wei, X. Pang, M. Zhou, K. Gao, *Corros. Sci.* 121 (2017): p. 57.

9. Y.S. Choi, S. Nešić, D. Young, *Environ. Sci. Technol.* 44 (2010): p. 9233.
10. Y.S. Choi, S. Nešić, "Effect of Water Content on the Corrosion Behavior of Carbon Steel in Supercritical CO₂ Phase with Impurities," CORROSION 2011, paper no. 11377 (Houston, TX: NACE International, 2011).
11. Y. Hua, R. Barker, A. Neville, *Int. J. Greenhouse Gas Control* 31 (2014): p. 48.
12. Y. Hua, R. Barker, A. Neville, *J. Supercrit Fluids* 97 (2015): p. 224.
13. M. Xu, W. Li, Y. Zhou, X. Yang, Z. Wang, Z. Li, *Int. J. Greenhouse Gas Control* 51 (2016): p. 357.
14. M. Xu, Q. Zhang, Z. Wang, J. Liu, Z. Li, *Corrosion* 73 (2017): p. 290.
15. M.F. Mohamed, A. Mohammed Nor, M.F. Suhor, M. Singer, Y.S. Choi, S. Nešić, "Water Chemistry for Corrosion Prediction in High-Pressure CO₂ Environments," CORROSION 2011, paper no. 11375 (Houston, TX: NACE, 2011).
16. A. Mohammed Nor, M.F. Suhor, M.F. Mohamed, M. Singer, S. Nešić, "Corrosion of Carbon Steel in High CO₂ Environment: Flow Effect," CORROSION 2011, paper no. 11245 (Houston, TX: NACE, 2011).
17. Y. Zhang, X. Pang, S. Qu, X. Li, K. Gao, *Int. J. Greenhouse Gas Control* 5 (2011): p. 1643.
18. A. Mohammad Nor, M.F. Suhor, M.F. Mohamed, M. Singer, S. Nešić, "Corrosion of Carbon Steel in High CO₂ Containing Environments: The Effect of High Flow Rate," CORROSION 2012, paper no. 0001683 (Houston, TX: NACE, 2012).
19. Y.S. Choi, D. Young, S. Nešić, L.G.S. Gray, *Int. J. Greenhouse Gas Control* 16S (2013): p. S70.
20. M. Seiersten, K.O. Kongshaug, "Materials Selection for Capture, Compression, Transport and Injection of CO₂," in *Carbon Dioxide Capture for Storage in Deep Geologic Formations*, eds. D.C. Thomas, S.M. Benson, vol. 2 (Oxford, UK: Elsevier Ltd., 2005), p. 937.
21. G. Heggum, T. Weydahl, M. Molnvik, A. Austegaard, "CO₂ Condition and Transportation," in *Carbon Dioxide Capture for Storage in Deep Geologic Formations*, eds. D.C. Thomas, S.M. Benson, vol. 2 (Oxford, UK: Elsevier Ltd., 2005), p. 925.
22. Y. Zhang, X. Pang, S. Qu, X. Li, K. Gao, *Corros. Sci.* 59 (2012): p. 186.
23. Y. Tang, X.P. Guo, G.A. Zhang, *Corros. Sci.* 118 (2017): p. 118.
24. S. Turgoose, G. John, M. Flynn, "Corrosion Inhibition in Supercritical Carbon Dioxide Systems Containing Water," CORROSION 2014, paper no. 4048 (Houston, TX: NACE, 2014).
25. Y. Zhang, K. Gao, G. Schmitt, "Inhibition of Steel Corrosion Under Aqueous Supercritical CO₂ Conditions," CORROSION 2011, paper no. 11379 (Houston, TX: NACE, 2011).
26. L. Wei, Z. Chen, X. Guo, *J. Electrochem. Soc.* 164 (2017): p. C602.
27. Y. Xiang, Z. Long, C. Li, H. Huang, X. He, *Int. J. Greenhouse Gas Control* 63 (2017): p. 141.
28. Mohd Farid Mohamed, "Water Chemistry and Corrosion Inhibition in High Pressure CO₂ Corrosion of Mild Steel" (Master's thesis, Ohio University, 2015).
29. T. Muraki, T. Hara, K. Nose, H. Asahi, "Effects of Chromium Content up to 5% and Dissolved Oxygen on CO₂ Corrosion," CORROSION 2002, paper no. 02272 (Houston, TX: NACE, 2002).
30. L. Xu, B. Wang, J. Zhu, W. Li, Z. Zheng, *Appl. Surf. Sci.* 379 (2016): p. 39.
31. Y.S. Choi, S. Hassani, T.N. Vu, S. Nešić, A.Z.B. Abas, *Corrosion* 72 (2016): p. 999.
32. L. Wei, X. Pang, K. Gao, *Corros. Sci.* 103 (2016): p. 132.
33. F. Pessu, R. Barker, A. Neville, *Corrosion* 73 (2017): p. 1168.
34. F. Pessu, Y. Hua, R. Barker, A. Neville, *Corrosion* 74 (2018): p. 886.
35. L. Wei, X. Pang, K. Gao, *Corros. Sci.* 111 (2016): p. 637.
36. Z. Liu, X. Gao, L. Du, J. Lia, P. Li, C. Yu, R.D.K. Misra, Y. Wang, *Electrochim. Acta* 232 (2017): p. 528.
37. P. Sui, J. Sun, Y. Hua, H. Liu, M. Zhou, Y. Zhang, J. Liu, Y. Wang, *Int. J. Greenhouse Gas Control* 73 (2018): p. 60.
38. C.M.C. Maya, "Effect of Wall Shear Stress on Corrosion Inhibitor Film Performance" (Ph.D. thesis, Ohio University, 2015).
39. Y. Zheng, "Electrochemical and Model of H₂S Corrosion of Carbon Steel" (Ph.D. thesis, Ohio University, 2015).
40. "High Temp & High Pressure pH Electrode," Corr Instruments, www.corrinstruments.com.
41. M.F. Suhor, M.F. Mohamed, A. Mohammad Nor, M. Singer, S. Nešić, "Corrosion of Mild Steel in High CO₂ Environment: Effect of the FeCO₃ Layer," CORROSION 2012, paper no. 0001434 (Houston, TX: NACE, 2012).
42. Y.S. Choi, F. Farelas, S. Nešić, A.A.O. Magalhães, C. de Azevedo Andrade, *Corrosion* 70 (2014): p. 38.
43. M. Kappes, G.S. Frankel, N. Sridhar, R.M. Carranza, *Corrosion* 68 (2012): p. 872.
44. S. Hassani, T.N. Vu, N.R. Rosli, S.N. Esmaeely, Y.S. Choi, D. Young, S. Nešić, *Int. J. Greenhouse Gas Control* 23 (2014): p. 30.
45. L.D. Paolinelli, T. Pérez, S.N. Simison, *Mater. Chem. Phys.* 126 (2011): p. 938.
46. T. Siu, C.Q. Jia, *Ind. Eng. Chem. Res.* 38 (1999): p. 1306.